

# Interface Modeling of Perovskite/Polymer Heterostructures for Enhanced Charge Transfer Efficiency in Hybrid Photovoltaic Materials

Somayyeh Alidoust<sup>1</sup> and V. Ongun Özçelik<sup>1, 2, \*</sup>

<sup>1</sup>Faculty of Engineering and Natural Sciences, Sabancı University, Istanbul, 34956 Turkey.

<sup>2</sup>Materials Science and Nano Engineering Program, Sabancı University, Istanbul, 34956 Turkey.

Perovskite solar cells (PSCs) based on methylammonium lead iodide (MAPbI<sub>3</sub>) exhibit remarkable photovoltaic performance, where interface engineering with hole transport layers (HTLs) is crucial for optimizing charge transfer and device efficiency. In this work, we present a density functional theory (DFT) study of the MAPbI<sub>3</sub>/poly(3-hexylthiophene) (P3HT) hybrid interface, focusing on the role of perovskite surface termination in determining interfacial stability and electronic structure. We model MAI- and PbI-terminated MAPbI<sub>3</sub> surfaces interfaced with P3HT and compare their interfacial electronic properties. Electronic structure calculations reveal distinct differences in orbital hybridization and band alignment: the MAI/m-P3HT interface exhibits weak coupling, whereas the PbI/m-P3HT interface shows stronger hybridization and enhanced charge transfer. Band alignment confirms type-II, hole-selective character in both cases, with more pronounced VBM adjustment for PbI. Charge difference maps, Bader analysis, and local density of states (LDOS) consistently indicate higher charge transfer and stronger electronic coupling for PbI termination. Electrostatic potential offsets and transport parameters further highlight termination-dependent differences, with lighter effective masses at PbI/m-P3HT and higher hole velocity at MAI/m-P3HT. These findings provide theoretical insight into interfacial charge transport mechanisms and offer guidelines for optimizing perovskite–organic hybrid solar cells.

## I. INTRODUCTION

Heterostructures formed by interfacing organic semiconducting polymers with stable substrates have gained significant attention for flexible electronics and photovoltaic technologies<sup>1–4</sup>. The contact between the polymer and the substrate surface often triggers spontaneous interfacial charge transfer, leading to electron–hole separation and redistribution of carriers, which reshapes the interfacial band structure via hybridization-driven charge accumulation<sup>5,6</sup>. The effectiveness of this charge transfer is highly sensitive to the atomic arrangement at the junction, interfacial electronic and chemical properties, polymer adsorption configuration, and hybridization strength, collectively setting the band alignment, carrier injection barriers, and contact resistance<sup>7,8</sup>. Among these heterostructures, perovskite based solar cells (PSCs) have emerged as a leading class of photovoltaic materials due to their high power conversion efficiencies (PCEs) (exceeding 27%), mechanically flexible optoelectronic properties, and compatibility with low-temperature, solution-based processing, which contributes to reduced fabrication costs<sup>9–11</sup>. For example, methylammonium lead iodide (CH<sub>3</sub>NH<sub>3</sub>PbI<sub>3</sub> or MAPbI<sub>3</sub>), which has a band gap of 1.55 eV, was first employed in liquid dye-sensitized solar cells in 2009, sparking a rapid surge in scientific research aimed at discovering improved perovskite materials for solar cells<sup>12</sup>. Just like MAPbI<sub>3</sub>, PSC materials typically adopt the ABX<sub>3</sub> perovskite structure, where A is a monovalent cation, B is a divalent metal cation, and X is a halide anion. The choice of each component directly affects the crystal stability, band gap, and overall optoelectronic performance of the perovskite. These characteristics make ABX<sub>3</sub> perovskites highly effective as an absorber layers in solar cell

applications.

In a typical PSC, the perovskite layer is sandwiched between electron and hole transport layers (ETL and HTL), which are crucial for efficient charge extraction. The performance of a PSC is heavily influenced by the interfaces between the perovskite layer and both the ETL and HTL, where energy level alignment, charge carrier mobility, and interfacial recombination play key roles in determining device efficiency and stability. Numerous studies on PSC devices have appeared in the literature, aiming to enhance power conversion efficiency, stability, and scalability, where these efforts have mainly focused on optimizing the perovskite absorber layer and improving the charge transport layers, including both the HTL and ETL<sup>13–20</sup>. For the perovskite layer, strategies such as MA, Pb, and I-site substitution have been widely explored. For example, formamidinium lead iodide (FAPbI<sub>3</sub>) has been developed to MA for improved thermal stability<sup>13</sup>. Similarly, potassium germanium chloride (KGeCl<sub>3</sub>) represents an approach to substitute lead with less toxic metals like germanium, while also demonstrating promising photovoltaic performance with relatively high PCE<sup>14</sup>. Additionally, mixed-cation and mixed-halide perovskites, such as (MA,FA)PbI<sub>3</sub><sup>21</sup> or (FA,Cs)Pb(I,Br)<sub>3</sub><sup>22</sup>, have been investigated to enhance phase stability and tune optoelectronic properties. For the ETL, various materials have been utilized, including inorganic semiconductors such as ZnO and TiO<sub>2</sub>, along with organic compounds like [6,6]-phenyl-C<sub>61</sub>-butyric acid methyl ester (PCBM) and C<sub>60</sub><sup>20</sup>. The HTLs can enhance hole extraction and affect the open-circuit voltage V<sub>oc</sub> by increasing hole concentration at the contact since V<sub>oc</sub> of PSCs is governed by the quasi-Fermi level difference at the interfaces<sup>23</sup>. Organic HTLs such as poly(3,4-ethylenedioxythiophene):poly(styrenesulfonate)

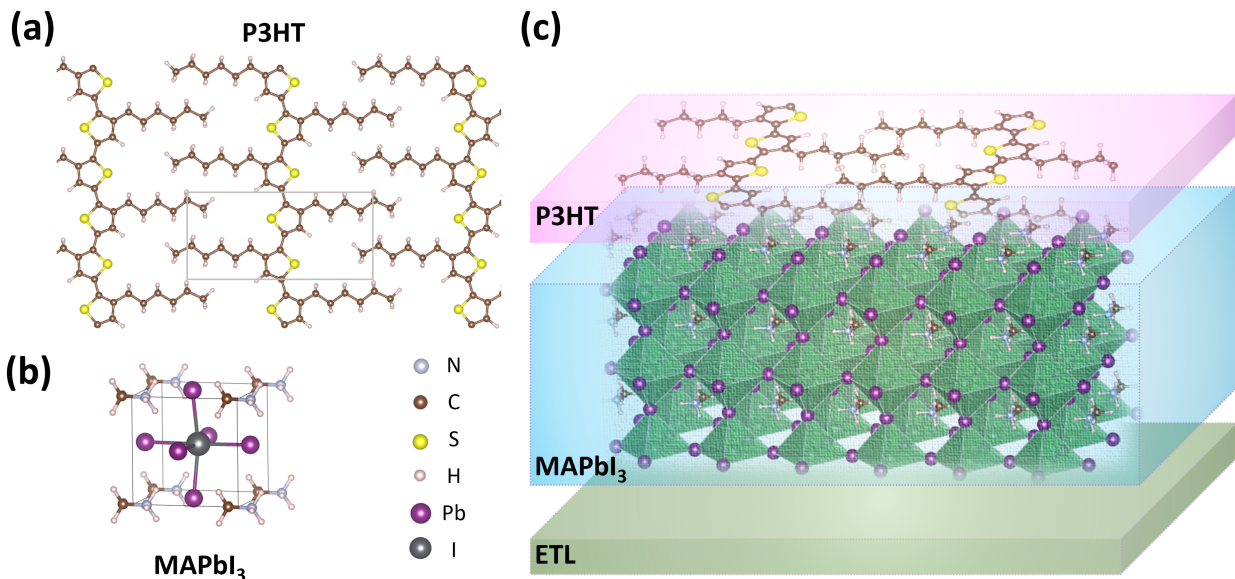


FIG. 1: (a) 2D periodic structure of P3HT. (b) 3D crystal structure of MAPbI<sub>3</sub>. (c) Schematic illustration of the MAPbI<sub>3</sub>/P3HT interface used in this study.

(PEDOT:PSS) and Spiro-OMeTAD are common choices, while inorganic alternatives like CuI, NiO, and Cu<sub>2</sub>O-doped Spiro-OMeTAD have also been investigated to enhance hole mobility and device longevity<sup>17,18</sup>.

Poly(3-hexylthiophene) (P3HT) is a benchmark semiconducting conjugated polymer extensively employed in organic photovoltaic and solar cell technologies due to its favorable charge-transport characteristics, ease of solution-based processing, and adjustable optoelectronic properties<sup>24–29</sup>. Due to the high cost of conventional HTLs like Spiro-OMeTAD, P3HT has been explored as a cost-effective alternative in PSCs<sup>30–32</sup>. Recent studies have shown that modifications, blends, and interface engineering with the perovskite layer can enhance its charge transport properties<sup>30–32</sup>. An additive-assisted strategy using P3HT in the perovskite precursor solution enhances film crystallinity, reduces defects, and creates a favorable perovskite/P3HT heterojunction, leading to improved hole extraction and increased PCE, from 12.72% to 15.57% in rigid and 11.81% to 13.54% in flexible devices<sup>31</sup>. Xu et al.<sup>32</sup> proposed constructing a molecular bridge at the P3HT/perovskite interface, which significantly enhances both the efficiency and stability of the resulting solar cells. This approach facilitates improved hole extraction, suppresses interfacial recombination, and passivates interfacial defects, leading to devices that demonstrate competitive PCEs alongside enhanced operational stability under ambient conditions<sup>32</sup>.

In this study, we focus on the interfacial optoelectronic properties of the MAPbI<sub>3</sub>/P3HT system, shown in Figure 1, using theoretical methods to better understand charge transfer behavior and band alignment at the interface.

We select MAPbI<sub>3</sub> as the perovskite material due to its well-established role as a benchmark in perovskite solar cell research. Its high PCE and extensive prior characterization make it an ideal reference point for studying interfacial properties and charge transport mechanisms. This approach can be extended to other perovskite compositions with reduced toxicity through B-site substitution, and can further be used to investigate how variations in the A-, B- and X-sites components influence interfacial behavior. We model the interfaces with different surface terminations, specifically MAI- and PbI<sub>2</sub>-terminated surfaces, to examine how termination affects the electronic coupling at the junction. This work offers a theoretical framework which has not yet been systematically explored for this type of interface. Using density functional theory (DFT), we compute band structures, band alignments, and charge transport characteristics, providing a comparative analysis between different terminations. Our results reveal clear interactions at the interface, including hybridization of states, which impact charge transfer dynamics and alignment. These findings offer valuable insight into the design of perovskite–organic hybrid solar cells and guide future efforts toward optimizing interfacial charge separation and transport.

## II. METHODS

All first-principles calculations were performed using the Vienna Ab initio Simulation Package (VASP)<sup>38</sup>. The electronic structure was treated

within the generalized gradient approximation using the Perdew–Burke–Ernzerhof (PBE)<sup>39</sup> exchange–correlation functional. Long-range dispersion interactions were included through the DFT-D3 correction<sup>40</sup>. Projector-augmented-wave (PAW) pseudopotentials<sup>41</sup> were employed to describe the electron–ion interactions. For each structure, full geometry optimizations were performed by relaxing all atomic positions and the cell volume, while keeping the lattice angles fixed to preserve the overall cell shape. The plane-wave basis set was expanded using an energy cutoff of 500 eV. A k-point mesh with approximately 40 points along each periodic direction was used to ensure convergence. The electronic self-consistency criterion was set to  $10^{-5}$  eV, and ionic relaxations were continued until the residual forces on all atoms were below  $10^{-3}$  eV/Å. Spin–orbit coupling (SOC) and hybrid exchange–correlation functionals were not applied. Although we are aware that the PBE functional underestimates the band gap, the very large number of atoms in our interface models made the inclusion of SOC or hybrid functional calculations computationally prohibitive. A vacuum spacing of 30 Å was introduced along the non-periodic direction to eliminate spurious interactions between periodic images, and dipole corrections were applied along the non-periodic direction to eliminate artificial electrostatic interactions in the systems. All static electronic-structure calculations, including the projected density of states, charge-density differences, and Bader charge analysis, were performed using VASP in conjunction with VASPKIT<sup>42</sup> and PyProcar<sup>43</sup>.

### III. RESULTS AND DISCUSSION

To support the analysis of interface stability, three terminations of pseudocubic triclinic *P1* structure of MAPbI<sub>3</sub><sup>33</sup> perovskite were considered, as shown in Figure 2a, for the calculation of cohesive energy ( $E_{coh}$ ) and the selection of suitable terminations for subsequent interface modeling. These were selected from among the variety of surface terminations considered in previous studies<sup>34–36</sup>. The terminations correspond to different surface layers: one terminated by methylammonium and iodide ions, referred to as MAI, and two terminated by lead and iodide ions with distinct atomic arrangements, labeled PbI<sub>a</sub> (PbI<sub>5</sub>) and PbI<sub>b</sub> (PbI<sub>6</sub>). Notably, Matta et al.<sup>34</sup> also employed the MAI and PbI<sub>a</sub> surfaces in their investigation of the perovskite/HTL interface. Here, we revisit these specific terminations to provide a comparative assessment based on cohesive energy.

The cohesive energy for each slab was computed using the following formula:

$$E_{coh} = \frac{E_{slab} - \sum_i n_i E_i^{\text{atom}}}{N} \quad (1)$$

where  $E_{slab}$  is the total energy of the slab,  $E_i^{\text{atom}}$  is the

reference energy of each isolated atom,  $n_i$  is the number of atoms of type i, and N is the total number of atoms in the slab. Figure 2b shows the calculated cohesive energy per atom for different surface terminations of the perovskite slab. Lower negative values (higher magnitude) indicate higher cohesive energy and greater thermodynamic stability. Among the considered terminations, MAI (3.35 eV/atom) and PbI<sub>a</sub> (3.26 eV/atom) exhibit slightly higher cohesive energies compared to PbI<sub>b</sub> (3.03 eV/atom), suggesting a marginally higher stability. Although the energy difference is not substantial, we focus on the MAI and PbI<sub>a</sub> terminations in the following analysis to reduce computational complexity and to prioritize the most stable configurations.

To form a commensurate heterostructure, three formula units of the selected MAPbI<sub>3</sub> termination were used as the perovskite slab, together with one formula unit of P3HT. As explained in detail in the Supporting Information (SI), P3HT was modified to match the dimensions of the three-unit MAPbI<sub>3</sub> layer. In the modified P3HT (m-P3HT), bond lengths and angles were altered compared to the pristine form. An initial vertical separation of 3.0 Å was introduced between the two materials prior to relaxation. The interface was then subjected to vertical distance optimization to determine the most favorable interlayer separation. Specifically, the distance between the m-P3HT layer and the perovskite surface was systematically varied from 2.5 Å to 5.0 Å. As shown in Figure 2c, the total energy reached a minimum at a vertical separation of 3.5 Å, indicating the optimal distance for interfacial interaction. The optimized structures of the two resulting interfaces (MAI- and PbI<sub>a</sub>-terminated) are shown in Figure 2d and 2e. An equilibrium distance of approximately 3.5 Å typically suggests a weak non-covalent interaction—most likely dominated by van der Waals forces—rather than strong chemical bonding, which usually occurs at shorter distances.

To further investigate the electronic interactions at the interface, we analyzed the projected band structure of the MAI/m-P3HT and PbI<sub>a</sub>/m-P3HT systems. Figure 3 reveals distinct contributions to the VBM and conduction CBM in the two interfaces. In the MAI/m-P3HT configuration, only the perovskite contributes near the band edges specifically, the VBM is primarily composed of iodine *p*-orbitals, while the CBM is dominated by lead *p*-orbitals. This indicates minimal interaction or hybridization between m-P3HT and the perovskite states near the Fermi level. In contrast, the PbI<sub>a</sub>/m-P3HT interface exhibits noticeable orbital contributions from both materials. The VBM includes significant input from the carbon *p*-orbitals of the m-P3HT layer, with additional contribution from the iodine *p*-orbitals of the perovskite at slightly lower energy levels, while the CBM retains iodine character from the perovskite. This suggests stronger interfacial coupling in the PbI<sub>a</sub>-terminated system, potentially facilitating improved charge transfer across the interface.

Band alignment analysis of the MAI/m-P3HT and

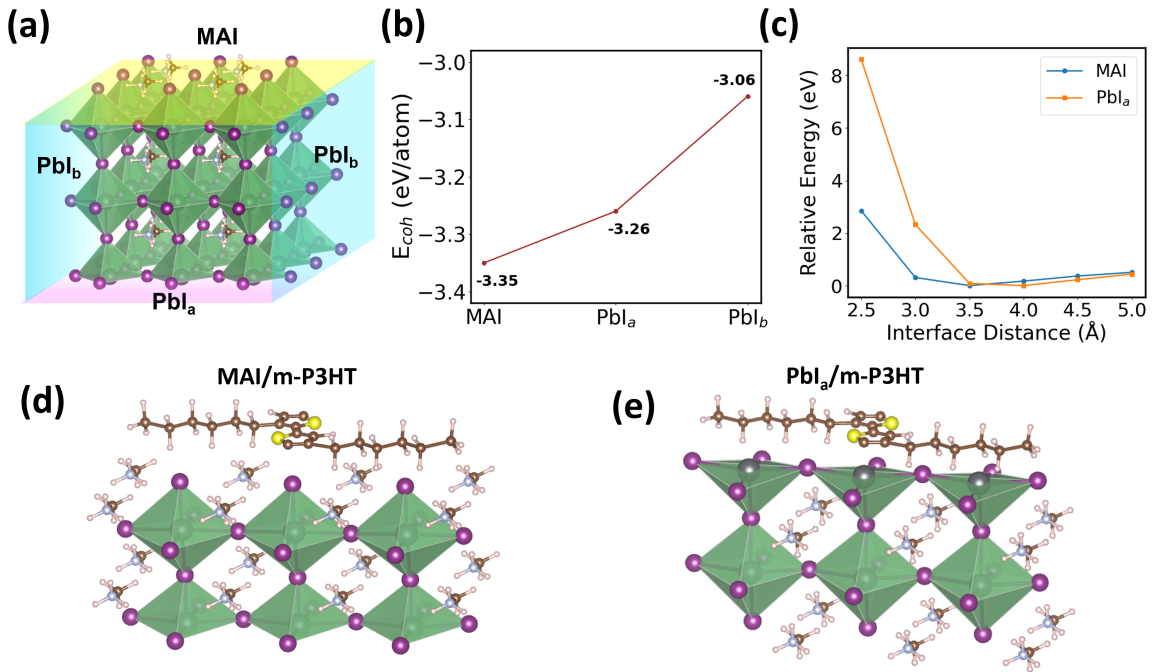


FIG. 2: (a) MAI, PbI<sub>a</sub>, and PbI<sub>b</sub> terminations of MAPbI<sub>3</sub> used for the P3HT interface study. (b) Cohesive energy per atom for each termination; lower values indicate greater stability. (c) Relative total energy versus distance between perovskite surface and m-P3HT; minima mark optimal interface separations. (d,e) Optimized structures of MAPbI<sub>3</sub>/m-P3HT interfaces for MAI- and PbI<sub>a</sub>-terminations, respectively..

PbI<sub>a</sub>/m-P3HT interfaces reveals notable differences in energy level alignment that influence charge transport across the interface, as shown in Figure 4. Both interfaces exhibit type-II band alignment<sup>37</sup> and are hole-selective. In both cases, the perovskite CBM lies far below the P3HT CBM ( $\Delta E \geq 3$  eV), ensuring efficient electron blocking. For the MAI/m-P3HT interface, the bands are positioned deeper compared to the PbI<sub>a</sub>/m-P3HT case, and the interface VBM and CBM remain almost unchanged with respect to the modified perovskite, consistent with the band structure results. In contrast, at the PbI<sub>a</sub>/m-P3HT interface, the VBM shows stronger adjustment and appears influenced by both the perovskite and P3HT states, leading to a more noticeable modification of the interface levels and efficient hole extraction. In addition, the figure also includes the pristine band edges of the pure materials, which allows a direct comparison between the pristine and modified structures and highlights the interfacial effects.

To understand the redistribution of electron density upon interface formation, charge difference analysis is carried out and calculated as:

$$\Delta\rho = \rho_{\text{interface}} - \rho_{\text{perovskite}} - \rho_{\text{m-P3HT}} \quad (2)$$

where  $\rho_{\text{interface}}$  is the electron density of the combined system, and  $\rho_{\text{perovskite}}$  and  $\rho_{\text{m-P3HT}}$  are the electron densities of the isolated components in the same geometry. This difference highlights regions of charge

accumulation and depletion at the interface. Figure 5 shows the charge difference analysis, along with Bader charge results that quantitatively partition the electron density among atoms to estimate net charge transfer and reveal the extent of charge rearrangement at the interface. The Bader charges indicate a slightly higher charge transfer at the PbI<sub>a</sub>/m-P3HT interface (0.10 e/f.u. or  $6.88 \times 10^{-4}$  e/Å) compared to the MAI/m-P3HT interface (0.05 e/f.u. or  $3.45 \times 10^{-4}$  e/Å), consistent with moderately stronger interfacial electronic interactions in the PbI<sub>a</sub>-terminated system.

In addition to the charge difference and Bader charge analyses, the local density of states (LDOS) profiles further elucidate the spatial distribution of electronic states along the out-of-plane direction (z-axis). As shown in Figure 5, the LDOS at the MAI/m-P3HT interface is mainly localized within the perovskite slab, with only a weak extension into the molecular region. In contrast, the PbI<sub>a</sub>/m-P3HT interface exhibits a more pronounced LDOS intensity at the boundary and a stronger extension toward the m-P3HT side. This result supports the larger Bader charge transfer and indicates enhanced electronic coupling at the PbI<sub>a</sub>-terminated interface.

To ensure reliable extraction of interfacial electronic properties, we analyzed the planar-averaged electrostatic potential along the z-direction. As shown in Fig.6, the potential profiles for MAI/m-P3HT and PbI<sub>a</sub>/m-P3HT exhibit pronounced oscillations within the  $z \approx 0-16$  Å

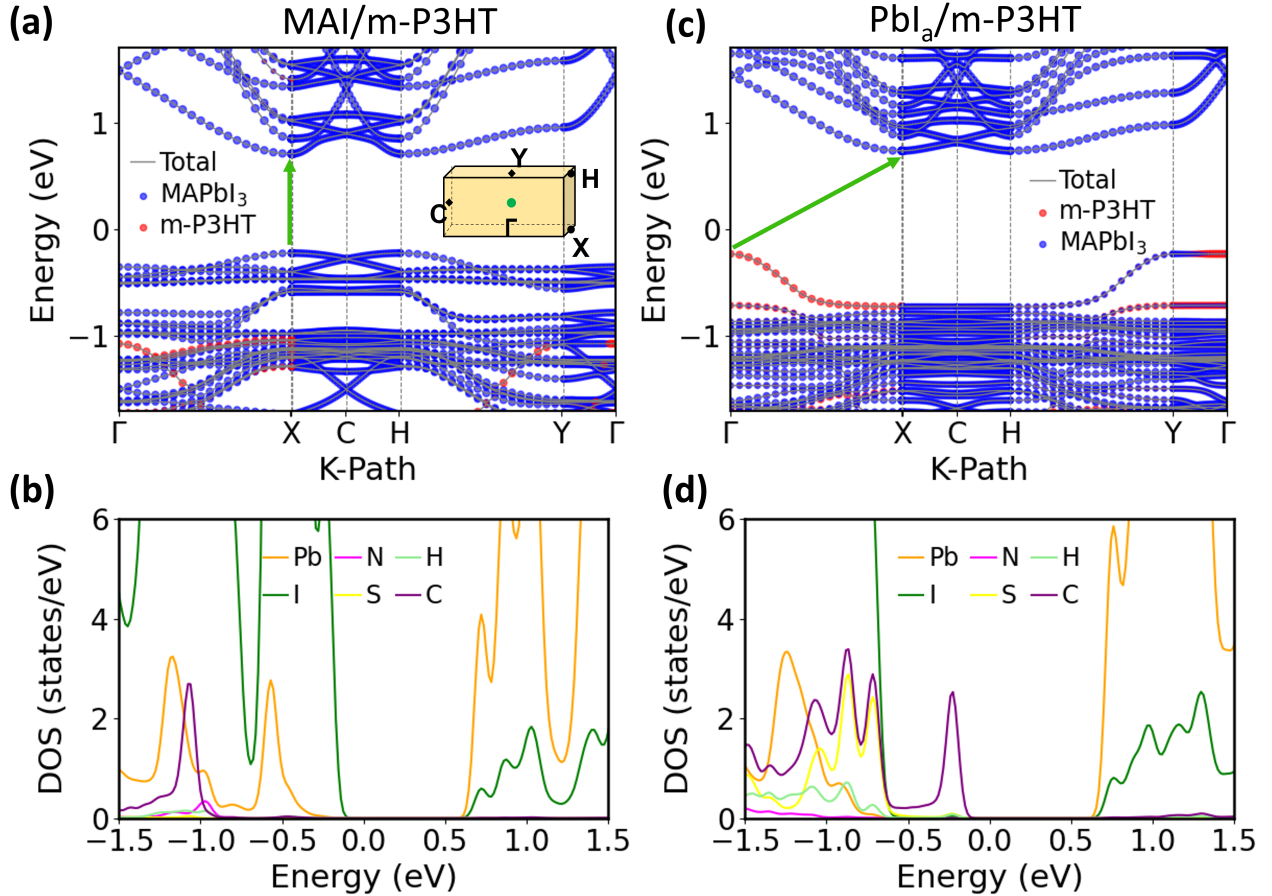


FIG. 3: (a, b) Projected band structure and density of states of the MAI/m-P3HT interface (band gap = 0.93 eV), and (c, d) those of the  $\text{PbI}_a$ /m-P3HT interface (band gap = 0.97 eV), illustrating the electronic contributions from each component.

range, reflecting the periodic arrangement of atomic layers in the  $\text{MAPbI}_3$  slab and the m-P3HT layer. Upon reaching the interfacial region, the oscillations are smoothed, and distinct potential offsets emerge between the perovskite and m-P3HT domains. The extracted potential energy differences ( $\Delta V$ ) indicate a larger offset for the MAI/m-P3HT interface ( $-2.7$  eV) compared to the  $\text{PbI}_a$ /m-P3HT interface ( $0.23$  eV). These values highlight the sensitivity of interfacial energetics to surface termination and provide direct insight into the band alignment and charge transfer characteristics at the perovskite/organic interface.

The charge carrier transport properties at the MAI/m-P3HT and  $\text{PbI}_a$ /m-P3HT interfaces were evaluated by analyzing the effective masses and Fermi velocities of electrons and holes. As shown in Table I, both interfaces exhibit comparable electron Fermi velocities, while the hole Fermi velocity is higher at the MAI/m-P3HT interface. The effective masses show a clear difference: carriers are heavier at the MAI/m-P3HT interface ( $m_e^* = 1.30$ ,  $m_h^* = 1.11$ ) compared to the  $\text{PbI}_a$ /m-P3HT interface ( $m_e^* = 0.73$ ,  $m_h^* = 0.31$ ), indicating more dispersive

bands in the latter case, especially for holes. These results suggest distinct transport characteristics depending on the interface termination, with lighter effective masses at  $\text{PbI}_a$ /m-P3HT and higher hole velocity at MAI/m-P3HT, reflecting different electronic structure modifications at the two interfaces.

TABLE I: Effective masses ( $m^*$ , in units of  $m_0$ ) and Fermi velocities ( $v_F$ , in units of  $10^6$  m/s) for electrons and holes at the MAI and  $\text{PbI}_a$  interfaces.

Interface	$m_{\text{electron}}^*$	$m_{\text{hole}}^*$	$v_{F,\text{electron}}$	$v_{F,\text{hole}}$
MAI/m-P3HT	1.30	1.11	1.72	1.87
$\text{PbI}_a$ /m-P3HT	0.73	0.31	1.73	1.39

#### IV. CONCLUSION

In this conclusion, here we investigated the interfacial electronic properties of  $\text{MAPbI}_3$ /P3HT heterojunctions with MAI- and  $\text{PbI}_a$ -terminated surfaces using first-

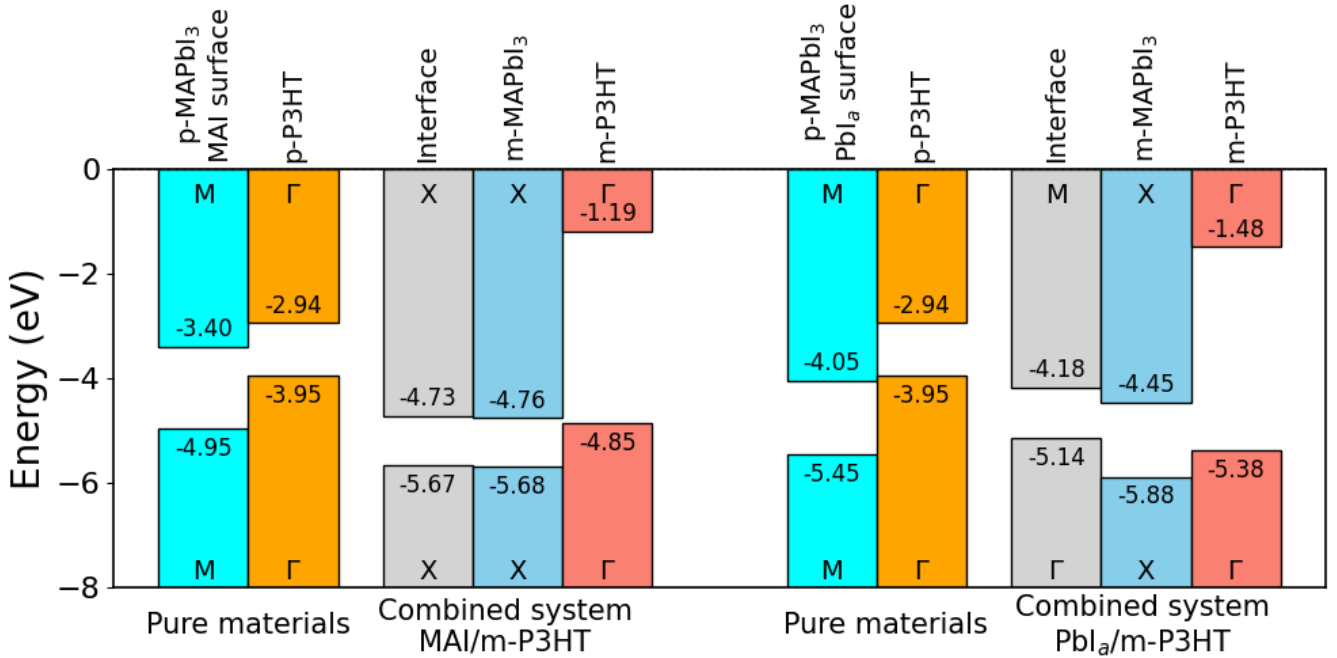


FIG. 4: Band alignment of the MAI/m-P3HT and  $\text{PbI}_a$ /m-P3HT interfaces, both exhibiting type-II alignment. Gray bars represent the interface band edges, while skyblue and salmon bars indicate the modified perovskite (m-MAPbI<sub>3</sub>) and modified P3HT (m-P3HT) band edges at the interface, respectively. Cyan and orange bars correspond to the pure perovskite (p-MAPbI<sub>3</sub> with MAI and  $\text{PbI}_a$  terminations) and pure P3HT (p-P3HT), included for comparison.

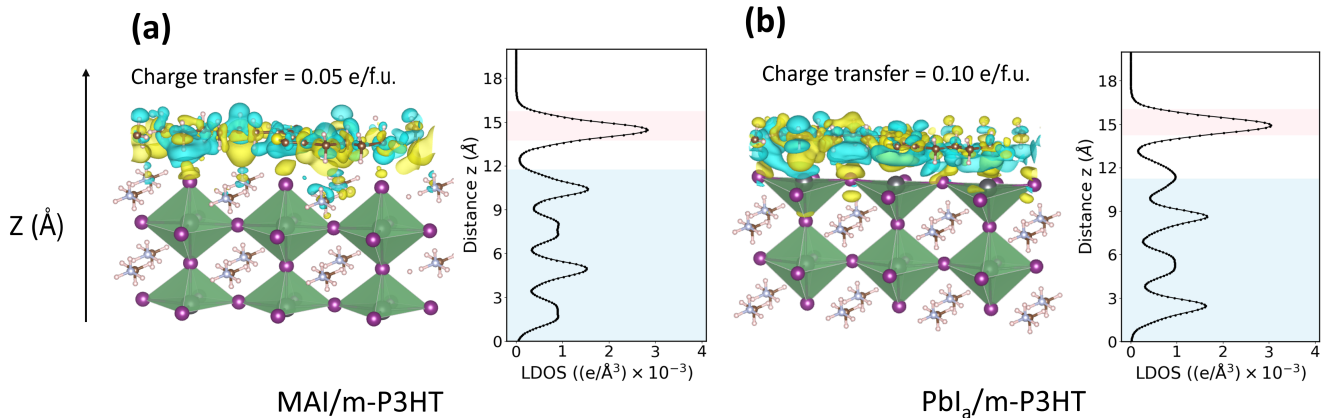


FIG. 5: Charge density difference maps showing electron accumulation (yellow) and depletion (cyan) at the (a) MAI/m-P3HT and (b)  $\text{PbI}_a$ /m-P3HT interfaces. LDOS profiles, also shown here, reveal stronger interfacial coupling and charge delocalization in  $\text{PbI}_a$  termination, supporting higher charge transfer and improved hole extraction.

principles calculations. Cohesive energy analysis confirmed the relative stability of MAI and  $\text{PbI}_a$  terminations, while structural optimization revealed an equilibrium interface distance of 3.5 Å, consistent with van der Waals interactions. Electronic structure calculations demonstrated that the MAI/m-P3HT interface exhibits weak coupling, whereas the  $\text{PbI}_a$ /m-P3HT interface shows stronger hybridization and enhanced charge transfer. Band alignment analysis indicated type-II,

hole-selective behavior for both interfaces, with improved VBM adjustment at the  $\text{PbI}_a$  termination. Charge density differences, Bader charges, and LDOS profiles further supported the stronger interfacial electronic interactions in  $\text{PbI}_a$ /m-P3HT. Finally, transport analysis revealed lighter effective masses at the  $\text{PbI}_a$  interface and higher hole velocity at the MAI interface, reflecting complementary charge transport characteristics. Overall, this theoretical insight provides a foundation for rational interface

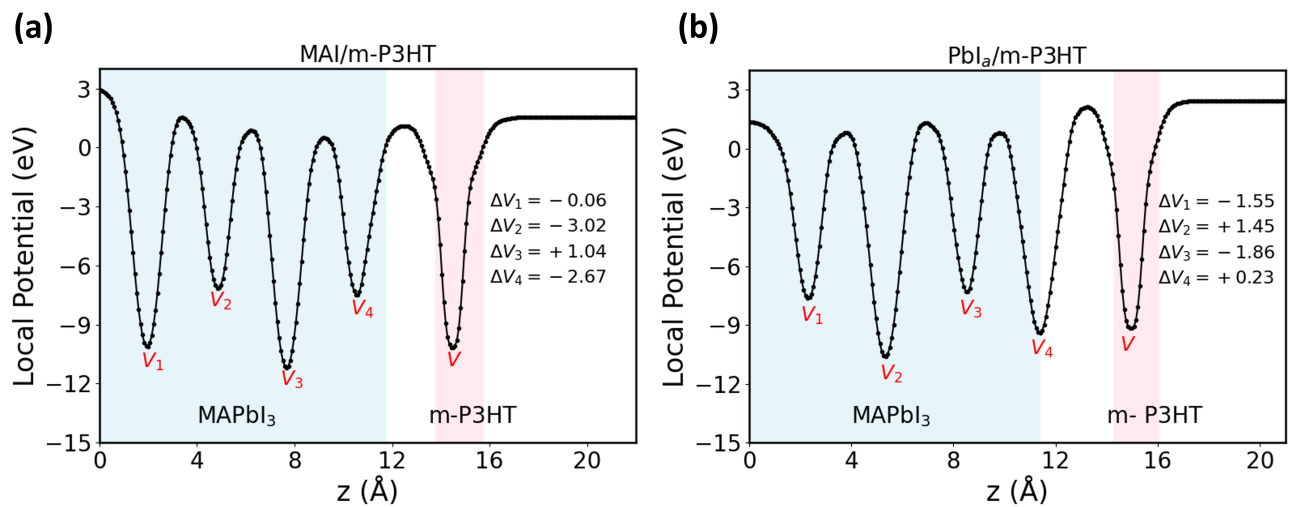


FIG. 6: Planar-averaged electrostatic potential along the z-direction for the (a) MAI/m-P3HT and (b)  $\text{PbI}_a$ /m-P3HT interfaces, along with the corresponding potential energy differences at the perovskite/m-P3HT interfaces. Shaded regions in blue and red indicate the  $\text{MAPbI}_3$  and P3HT slabs, respectively.

design in PSCs employing P3HT HTLs, guiding future efforts to optimize charge extraction and device performance.

#### Acknowledgements

We acknowledge funding from the Scientific and Technological Research Council of Turkey (TUBITAK) under

project no 123F264. Computational resources have been provided by TUBITAK ULAKBIM, High Performance and Grid Computing Center and by the National Center for High Performance Computing of Turkey (UHeM) under grant numbers 1013432022.

\* Electronic address: [ongun.ozcelik@sabanciuniv.edu](mailto:ongun.ozcelik@sabanciuniv.edu)

<sup>1</sup> Sang-Hoon Bae, Hyun Kum, Wei Kong, Yunjo Kim, Chanyeol Choi, Byunghun Lee, Peng Lin, Yongmo Park, and Jeehwan Kim. Integration of bulk materials with two-dimensional materials for physical coupling and applications. *Nat. Mater.*, 18(6):550, 2019.

<sup>2</sup> Wendy U Huynh, Janke J Dittmer, and A Paul Alivisatos. Hybrid nanorod-polymer solar cells. *Science*, 295(5564):2425–2427, 2002.

<sup>3</sup> Jeong Ah Chang, Jae Hui Rhee, Sang Hyuk Im, Yong Hui Lee, Hi-jung Kim, Sang Il Seok, Md K Nazeeruddin, and Michael Gratzel. High-performance nanostructured inorganic-organic heterojunction solar cells. *Nano Lett.*, 10(7):2609–2612, 2010.

<sup>4</sup> V. O. Özçelik, Y. Li, W. Xiong, and F. Paesani. Modeling spontaneous charge transfer at metal/organic hybrid heterostructures. *Journal of Physical Chemistry C*, 124(8):4802–4809, Feb 2020.

<sup>5</sup> Bo Xiang, Yingmin Li, C Huy Pham, Francesco Paesani, and Wei Xiong. Ultrafast direct electron transfer at organic semiconductor and metal interfaces. *Sci. Adv.*, 3(11):e1701508, 2017.

<sup>6</sup> Slawomir Braun, William R Salaneck, and Mats

Fahlman. Energy-level alignment at organic/metal and organic/organic interfaces. *Adv. Mater.*, 21(14–15):1450–1472, 2009.

<sup>7</sup> S Dag and Lin-Wang Wang. Modeling of nanoscale morphology of regioregular poly (3-hexylthiophene) on a zno (1010) surface. *Nano Lett.*, 8(12):4185–4190, 2008.

<sup>8</sup> Sefa Dag and Lin-Wang Wang. Packing structure of poly (3-hexylthiophene) crystal: ab initio and molecular dynamics studies. *The Journal of Physical Chemistry B*, 114(18):5997–6000, 2010.

<sup>9</sup> Giulia Grancini and Mohammad Khaja Nazeeruddin. Dimensional tailoring of hybrid perovskites for photovoltaics. *Nat. Rev. Mater.*, 4(1):4–22, Jan 2019.

<sup>10</sup> Colin Tynnik, James Lee, Jeni Sorli, Xiaojie Liu, Emma K. Holland, Cynthia S. Day, John E. Anthony, Yueh-Lin Loo, Z. Valy Vardeny, and Oana D. Jurchescu. Photocurrent in metal-halide perovskite/organic semiconductor heterostructures: Impact of microstructure on charge generation efficiency. *ACS Appl. Mater. Interfaces*, 13(8):10231–10238, Mar 2021.

<sup>11</sup> Best research-cell efficiency chart. visited on 2023-11-20.

<sup>12</sup> Akihiro Kojima, Kenjiro Teshima, Yasuo Shirai, and Tsutomu Miyasaka. Organometal halide perovskites as visible-

light sensitizers for photovoltaic cells. *J. Am. Chem. Soc.*, 131(17):6050–6051, May 2009.

<sup>13</sup> Emanuele Smecca, Youhei Numata, Ioannis Deretzis, Giovanna Pellegrino, Simona Boninelli, Tsutomu Miyasaka, Antonino La Magna, and Alessandra Alberti. Stability of solution-processed mapbi<sub>3</sub> and fapbi<sub>3</sub> layers. *Phys. Chem. Chem. Phys.*, 18:13413–13422, 2016.

<sup>14</sup> Ubaid Ur Rehman, Rasmiah S. Almufarij, A.R. Abd-Elwahed, Kashaf Ul Sahar, Ejaz Hussain, Arslan Ashfaq, Khalid Mahmood, and Chun-Ming Wang. Improving efficiency of germanium-based perovskite solar cells with graphene interface layer: A strategy to minimize charge recombination. *Journal of Physics and Chemistry of Solids*, 198:112487, 2025.

<sup>15</sup> Md. Faruk Hossain, Md. Mahabur Rahman, Md. Harun-Or-Rashid, Mongi Amami, Lamia Ben Farhat, and Md. Ferdous Rahman. Probing the impact of four bsf layers on masni<sub>3</sub>-based lead-free perovskite solar cells for ~33% efficiency. *Advanced Theory and Simulations*, 8(1):2400662, 2025.

<sup>16</sup> Somayyeh Alidoust, Fatemeh Jamalinabijan, and Adem Tekin. Light-harvesting lead-free mixed cation hybrid halide perovskites: A density functional theory-based computational screening study. *ACS Applied Energy Materials*, 7, 01 2024.

<sup>17</sup> Song Li, Yong-Li Cao, Wen-Hua Li, and Zhi-Shan Bo. A brief review of hole transporting materials commonly used in perovskite solar cells. *Rare Metals*, 40(10):2712–2729, Oct 2021.

<sup>18</sup> Thi Muoi Vo, Thi My Huyen Nguyen, Rui He, and Chung Wung Bark. Harnessing cu<sub>2</sub>O-doped 4-tert-butylpyridine in spiro-ometad: Study on improved performance and longevity of perovskite solar cells. *ACS Omega*, 9(46):46030–46040, Nov 2024.

<sup>19</sup> Liang Chen, Linlin Qiu, Lixin Song, Yongfeng Yuan, Jie Xiong, and Pingfan Du. Cugao<sub>2</sub> nanosheets and cu-cro<sub>2</sub> nanoparticles mixed with spiro-ometad as the hole-transport layer in perovskite solar cells. *ACS Applied Nano Materials*, 5(5):7312–7320, May 2022.

<sup>20</sup> Marwa Dkhili, Giulia Lucarelli, Francesca De Rossi, Babak Taheri, Khadija Hammedi, Hatem Ezzaouia, Francesca Brunetti, and Thomas M. Brown. Attributes of high-performance electron transport layers for perovskite solar cells on flexible pet versus on glass. *ACS Applied Energy Materials*, 5(4):4096–4107, Apr 2022.

<sup>21</sup> Won-Gyu Choi, Sungjae Na, Chan-Gyu Park, and Taeho Moon. Organic-cation-mixed (fa,ma)pb<sub>3</sub> through sequential vapor growth for planar perovskite solar cells. *Solar Energy*, 178:56–60, 2019.

<sup>22</sup> Karl L. Heinze, Tobias Schulz, Roland Scheer, and Paul Pistor. Structural evolution of sequentially evaporated (cs,fa)pb(i,br)<sub>3</sub> perovskite thin films via in situ x-ray diffraction. *physica status solidi (a)*, 221(3):2300690, 2024.

<sup>23</sup> Robert J. E. Westbrook, Dr. Irene Sanchez-Molina, Dr. Jose Manuel Marin-Beloqui, Dr. Hugo Bronstein, and Dr. Saif A. Haque. Effect of interfacial energetics on charge transfer from lead halide perovskite to organic hole conductors. *The Journal of Physical Chemistry C*, 122(2):1326–1332, Jan 2018.

<sup>24</sup> Qian Liu, Zunfeng Liu, Xiaoyan Zhang, Liying Yang, Nan Zhang, Guiling Pan, Shougen Yin, Yongsheng Chen, and Jun Wei. Polymer photovoltaic cells based on solution-processable graphene and p3ht. *Advanced Functional Materials*, 19(6):894–904, 2009.

<sup>25</sup> Simone Fratini, Mark Nikolka, Alberto Salleo, Guillaume Schweicher, and Henning Sirringhaus. Charge transport in high-mobility conjugated polymers and molecular semiconductors. *Nature Materials*, 19(5):491–502, May 2020.

<sup>26</sup> A. Lücke, W. G. Schmidt, E. Rauls, F. Ortmann, and U. Gerstmann. Influence of structural defects and oxidation onto hole conductivity in p3ht. *Journal of Physical Chemistry B*, 119(21):6481–6491, May 2015.

<sup>27</sup> J. Liu et al. Oriented poly(3-hexylthiophene) nanofibril with the  $\pi$ - $\pi$  stacking growth direction by solvent directional evaporation. *Langmuir*, 27(7):4212–4219, Apr 2011.

<sup>28</sup> Vladimir Yu Rudyak, Alexey A Gavrilov, Daria V Guseva, Shih-Huang Tung, and Pavel V Komarov. Accounting for  $\pi$ - $\pi$  stacking interactions in the mesoscopic models of conjugated polymers. *Molecular Systems Design & Engineering*, 5(6):1137–1146, 2020.

<sup>29</sup> Saeed Mardi, Marialilia Pea, Andrea Notargiacomo, Narges Yaghoobi Nia, Aldo Di Carlo, and Andrea Reale. The molecular weight dependence of thermoelectric properties of poly (3-hexylthiophene). *Materials*, 13(6):1404, 2020.

<sup>30</sup> Pari Baraneehdaran, Sankar Sekar, Silambarasan Murugesan, Djaloud Ahamada, Syed Ali Beer Mohamed, Youngmin Lee, and Sejoon Lee. Recent advances and remaining challenges in perovskite solar cell components for innovative photovoltaics. *Nanomaterials (Basel)*, 14(23), November 2024.

<sup>31</sup> Haixia Xie, Jie Liu, Xingtian Yin, Yuxiao Guo, Dan Liu, Gangfeng Wang, and Wenxiu Que. Perovskite/p3ht graded heterojunction by an additive-assisted method for high-efficiency perovskite solar cells with carbon electrodes. *Colloids and Surfaces A: Physicochemical and Engineering Aspects*, 635:128072, 2022.

<sup>32</sup> Dongdong Xu, Zhiming Gong, Yue Jiang, Yancong Feng, Zhen Wang, Xingsen Gao, Xubing Lu, Guofu Zhou, Jun-Ming Liu, and Jinwei Gao. Constructing molecular bridge for high-efficiency and stable perovskite solar cells based on p3ht. *Nature Communications*, 13(1):7020, Nov 2022.

<sup>33</sup> WMD-group. Ch<sub>3</sub>nh<sub>3</sub>pb<sub>3</sub>.cif, 2014. GitHub repository.

<sup>34</sup> Sri Kasi Matta, Chunmei Zhang, Anthony P. O'Mullane, and Aijun Du. Density functional theory investigation of carbon dots as hole-transport material in perovskite solar cells. *ChemPhysChem*, 19(22):3018–3023, 2018.

<sup>35</sup> Yun Wang, Bobby G. Sumpter, Jingsong Huang, Haimin Zhang, Porun Liu, Huagui Yang, and Huijun Zhao. Density functional studies of stoichiometric surfaces of orthorhombic hybrid perovskite ch<sub>3</sub>nh<sub>3</sub>pb<sub>3</sub>. *The Journal of Physical Chemistry C*, 119(2):1136–1145, Jan 2015.

<sup>36</sup> Jun Haruyama, Keitaro Sodeyama, Liyuan Han, and Yoshitaka Tateyama. Surface properties of ch<sub>3</sub>nh<sub>3</sub>pb<sub>3</sub> for perovskite solar cells. *Accounts of Chemical Research*, 49(3):554–561, Mar 2016.

<sup>37</sup> V Ongun Özcelik, Javad G Azadani, Ce Yang, Steven J Koester, and Tony Low. Band alignment of two-dimensional semiconductors for designing heterostructures with momentum space matching. *Physical Review B*, 94(3):035125, 2016.

<sup>38</sup> G. Kresse and J. Furthmüller. Efficient iterative schemes for ab initio total-energy calculations using a plane-wave basis set. *Phys. Rev. B*, 54:11169–11186, Oct 1996.

<sup>39</sup> John P. Perdew, Kieron Burke, and Matthias Ernzerhof. Generalized gradient approximation made simple. *Phys. Rev. Lett.*, 77:3865–3868, Oct 1996.

<sup>40</sup> Justin S. Smith, Ben Nebgen, Nicholas Lubbers, Olexandr Isayev, and Adrian E. Roitberg. Less is more: Sampling chemical space with active learning. *The Journal of Chemical Physics*, 148(24):241733, 05 2018.

<sup>41</sup> P. E. Blöchl. Projector augmented-wave method. *Phys. Rev. B*, 50:17953–17979, Dec 1994.

<sup>42</sup> Vei Wang, Nan Xu, Jin-Cheng Liu, Gang Tang, and Wen-Tong Geng. Vaspkit: A user-friendly interface facilitating high-throughput computing and analysis using vasp code. *Computer Physics Communications*, 267:108033, 2021.

<sup>43</sup> Uthpala Herath, Pedram Tavadze, Xu He, Eric Bousquet, Sobhit Singh, Francisco Muñoz, and Aldo H. Romero. Pyprocar: A python library for electronic structure pre/post-processing. *Computer Physics Communications*, 251:107080, 2020.